Macromolecules **2007,** *40,* 3977−3989

Effect of Temperature and Annealing on the Phase Composition, Molecular Mobility, and the Thickness of Domains in Isotactic Polypropylene Studied by Proton Solid-State NMR, SAXS, and DSC

C. Hedesiu,[‡,§] D. E. Demco,[*,‡] R. Kleppinger,[§] G. Vanden Poel,[§] W. Gijsbers,[§]
B. Blümich,[‡] K. Remerie,[†] and V. M. Litvinov[*,§]

SABIC Europe BV, P.O. Box 319 6160 AH, Geleen, The Netherlands, Institut für Technische und Makromolekulare Chemie, Rheinisch-Westfälische Technische Hochschule, Worringer Weg 1, D-52056 Aachen, Germany, and DSM Research, P. O. Box 18, 6160 MD Geleen, The Netherlands

Received January 3, 2007; Revised Manuscript Received March 26, 2007

ABSTRACT: A combination of DSC, SAXS, WAXD, ^{1}H time-domain, and frequency domain NMR measurements was used for determining the amount of rigid/crystallinity, semirigid, and soft fractions of iPP. Changes in the rigid, semirigid, and soft fractions of isotactic polypropylene (iPP) were investigated as a function of temperature, annealing time, and annealing temperature. The most probable iPP morphology was established by TEM and by comparing ^{1}H spin-diffusion data with data from multidimensional solutions of the spin-diffusion equations. Proton NMR spin-diffusion method, which employs double-quantum (DQ) and Goldman−Shen dipolar filters, was used in order to provide the domain thickness in iPP. The temperature dependence of spin diffusivities was taken into account, and a semiquantitative theory is presented for this dependence in the case of amorphous domains. A combination of ^{1}H spin-diffusion NMR and SAXS was used to estimate the lamellar thicknesses for nonannealed and annealed iPP samples. Annealing at temperatures above 110 °C causes increases in the lamellar thickness and the crystallinity and a decrease in the chain mobility of rigid and semirigid fractions. The above quantities and the chain dynamics are reported for three annealing temperatures, 134, 143, and 153 °C, and an annealing time in the range of 15 min to 30 h. It is shown that the crystalline domains thickening during annealing of iPP can be described by a model based on irreversible thermodynamics. A phenomenological correlation is established between ^{1}H transverse magnetization relaxation rate of the rigid fraction of iPP and the annealing temperatures.

1. Introduction

The physical and mechanical properties of semicrystalline polymers (like isotactic polypropylene), and their practical lifetime, are significantly influenced by both the changes in the degree of crystallinity,[1−11] and the orientation distribution of the crystalline volume portion.[12,13] Both quantities typically change when the sample is exposed to temperatures well above the glass transition due to annealing.[14−22] This means that the degree of the crystallinity and the orientation distribution depend on processing conditions, crystallization, annealing and thermal history in such materials. It is known that the annealing of semicrystalline polymers after the fabrication causes changes in the structure and properties of the materials. This process has been employed to improve the final properties of the polymers via healing of defects and diminishing residual stress and strain. In addition, lamellae thickening and rearrangement of the chain during heating also occur upon annealing.

Various experimental methods have been used to determine the crystallinity, phase composition, mobility, and thickness of domains of semicrystalline polymers. The most frequently used methods for estimating the degree of crystallinity are differential scanning calorimetry (DSC),[23,24] density measurements,[25] X-ray diffraction,[5,26−30] and nuclear magnetic resonance (NMR).[20,31−38] Each of these methods is based on a different physical property, and gives rise to a different definition of the crystalline phase.[39] Although the degree of crystallinity is a quantitative concept, different measurement techniques on exactly the same sample do not always yield the same value. There are several reasons for these apparent differences. They can be attributed in the part to different selectivity of the various techniques to the two major regions. In addition, the contribution of the interface to the result of measurement must be taken into account. The NMR studies on semicrystalline polymers have shows the existence of an intermediate noncrystalline phase associated with the lamella structure.[20,35−38] This region is characterized by a degree of order perpendicular to the lamellae surface but disorder in the lateral direction. The interface is important from a theoretical viewpoint and is a key factor in determining the overall crystalline structure, the morphology, and, thus, the mechanical properties.

For establishing structure−property relationships of semicrystalline polymers, the characterization of lamellar thickness in bulk materials is a necessity, because their thermal and physical properties depend largely on the characteristic of the lamellae. Traditionally, transmission electron micrograph (TEM) and small-angle X-ray scattering (SAXS) are two major techniques used to determine the lamellar thickness. The former offers the advantage of direct access to the morphology. SAXS is a well-developed method to quantitatively determine the thicknesses of alternating layers of the crystalline and amorphous regions that are formed in semicrystalline polymers. The morphological parameters can be deduced from SAXS data based on a model calculation. No tedious sample preparation is required for SAXS measurements. Although an

---

[*] To whom correspondence should be addressed. E-mail: (D.E.D.) demco@mc.rwth-aachen.de; (V.M.L.) victor.litvinov@dsm.com.

[†] SABIC Europe BV.

[‡] Institut für Technische und Makromolekulare Chemie, Rheinisch-Westfälische Technische Hochschule.

[§] DSM Research.

10.1021/ma070014q CCC: $37.00

indirect approach is applied, SAXS provides volume average characteristic.

Proton NMR spin-diffusion experiments have been used to provide information about the thickness of domains with different molecular mobility in heterogeneous polymers[40,41] and polymer fibers.[42−45] Previous ^{1}H NMR spin-diffusion experiments have shown that the lamellae thickness of semicrystalline polymers varies in a wide range, depending on chain branching and thermal history of the sample.[41,46] The thickness of the rigid domains in semicrystalline polymers can differ from the lamellae thickness, as some fraction of interface and the soft phase can be largely immobilized and cause an apparent increase in the lamellae thickness.

The main aim of this work is to study the change in the rigid fraction/crystallinity, semirigid, and soft fractions, and lamellae thicknesses for both annealed and nonannealed iPP samples. This was done using a combination of DSC, SAXS, WAXD, TEM, and ^{1}H solid-state NMR, including spin-diffusion NMR. The ^{1}H NMR spin-diffusion methods, which explore both double-quantum (DQ) dipolar filter[47−49] and the Goldman−Shen (GS) filter,[50,51] was used for the first time to provide a more accurate analysis of the domain thickness of iPP. It is thought that TEM, SAXS, and NMR are complementary techniques, providing morphological evidence on the nanometer scale. The most probable morphology was established by comparing the ^{1}H spin-diffusion data with the multidimensional evaluation of the magnetization by spin-diffusion. The results are compared under the given conditions, which include the annealing time and annealing temperature. A simple model of crystal thickening as a function of the annealing time is discussed. The correlation between transverse relaxation rates and thickness of the rigid domain is presented, i.e., microscopic and mesoscopic properties.

2. Experimental Section

2.1. Sample Description and Preparation. Isotactic polypropylene homopolymer sample obtained from SABIC Europe BV was used in our experiments. The material was injected in an Engel 45A machine. The melt temperature was set to 235 °C, the holding pressure to 40 MPa, the holding time to 20 s, the cooling time to 20 s, and the overall cycle time to 49.5 s. For the annealing study, the sample was further annealed in the NMR probe at 134 143, and 153 °C, for several times between 15 min and 30 h.

2.2. DSC Measurements. The first and second melting and crystallization curves of (non)-annealed iPP were recorded on a Perkin-Elmer DSC7 at heating/cooling rates of 10 °C/min. The specific heat capacity measurements, presented in this article were performed in the way described by Mathot.[24]

2.3. Transmission Electron Microscopy (TEM). The lamellar morphology of iPP samples was studied by TEM. The injection-molded plate was trimmed at a temperature of −120 °C and stained for 24 h in a RuO_4 solution. Sections 70 nm thick were obtained by slicing the sample with an ultramicrotrome at −120 °C. Images were recorded with a Philips CM200 TEM at an acceleration voltage of 120 kV.

2.4. Small-Angle X-ray Scattering. Small-angle X-ray scattering (SAXS) experiments were performed with a modified Kratky setup attached to a conventional, sealed X-ray tube (40 kV and 50 mA), which provides line-focused Ni-filtered Cu Kα radiation (0.154 nm). The scattering signal was recorded with a MBraun 50 M position sensitive detector. The calibration was performed as described in ref 52.

2.5. NMR Measurements and Data Analysis. Different solid-state ^{1}H NMR methods, namely wide-line NMR spectroscopy, transverse magnetization relaxation (T_2 relaxation), and spin-diffusion experiments, were used to study the phase composition, the molecular mobility, and the domain thickness in iPP. The experiments were performed at low magnetic field using a Bruker Minispec MQ20 spectrometer operating at a proton resonance frequency of 19.6 MHz, and at high magnetic field using a Bruker DSX-500 MHz spectrometer operating at a proton resonance frequency of 500.45 MHz. The data were collected for static sample at temperatures between 25 and 140 °C. The measurements, as a function of increasing temperature, were performed from 10 min after thermal stabilization time at each temperature.

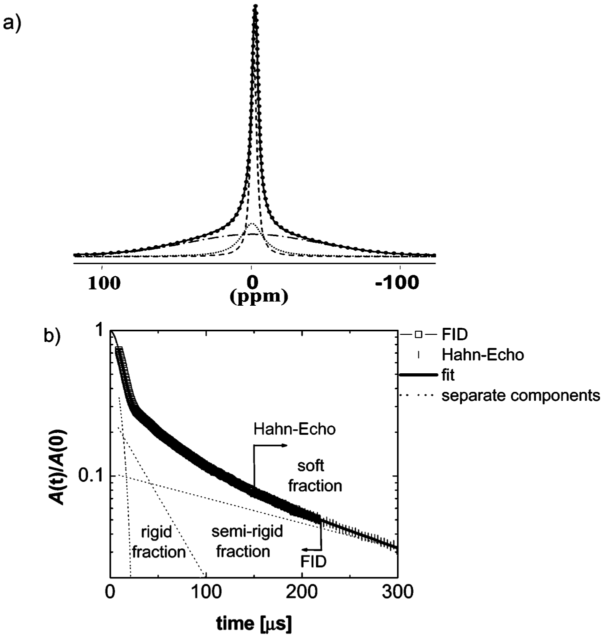

Figure 1. (a) Proton wide-line NMR spectra (solid line) of iPP measured at 70 °C with 500 MHz NMR spectrometer. The dashed lines show the spectral components that are assigned to the rigid, semirigid, and soft fractions of iPP—broad, intermediate, and narrow line widths, respectively. (b) The decay of the transverse magnetization relaxation (points) for iPP at 70 °C. The decay (FID) was measured at 20 MHz NMR spectrometer using the SPE (□) and the HEPS (I) methods. The solid line represents the result of a least-squares fit of the decay with a linear combination of the Abragam function and two exponential functions. Dotted lines show the separate components that are assigned to rigid, semirigid, and soft iPP fractions.

2.5.1. Proton Wide-Line NMR Spectroscopy. The NMR spectra measured at 500 MHz were deconvoluted into three components using the Bruker WinFit program. The line shape of the rigid component was taken as Gaussian, those of the semirigid and soft components were taken as a Lorentzian (Figure 1a). The errors in evaluation of the rigid fraction are not essentially substantiated by the approximation of the Gaussian line shape as compared with Abragam function. Because the Abragam function does not have an analytical Fourier transform the fit of the frequency domain spectra is difficult. At high magnetic field, the duration of a 90° pulses was 3 μs, the dead time was 3 μs, the dwell time was 0.75 μs, and the recycle delay was 5 s for all the experiments.

2.5.2. Proton Transverse Magnetization Relaxation (*T_2* Relaxation). At low magnetic field, the duration of a 90° pulse was 2.7−2.8 μs, the dead time was 7 μs, and the dwell time was 0.5 μs. A BVT-3000 temperature controller was used for temperature regulation with a temperature stability better than 1 °C. In order to measure the decay of the ^{1}H transverse magnetization (T_2 decay), from the rigid, semirigid, and soft fractions of the sample, three different NMR pulse sequences were used. In the first experiment, the free induction decay (FID) was recorded after a 90°-pulse excitation (SPE, single pulse excitation), i.e. $90°_x$−dead time−acquisition of the amplitude $A(t)$ of the transverse magnetization as a function of time t. The second experiment was the solid echo pulse sequence (SEPS), i.e., $90°_x - t_{se} - 90°_y - t_{se}$−acquisition of the amplitude of the transverse magnetization $A(t)$, with $t_{se} = 10$ μs. The third one was the Hahn-echo pulse sequence (HEPS), i.e. $90°_x - t_{He} - 180°_y - t_{He}$−acquisition of the amplitude of the echo maximum for variable value of $2t_{\mathrm{He}}$. The systematic errors inherent to the FID and SEPS methods are described in refs 52, 53, and 55

The Hahn-echo pulse sequence was used to avoid the effect of the inhomogeneity of the magnetic field on the decay of the transverse magnetization of the soft fraction of iPP, and to obtain reliable information about the molecular mobility and amount of the soft fraction. The 90° pulse excitation (SPE) and HEPS were finally used to record the FID for quantitative analysis of the phase composition. The results of both experiments were combined as described in ref 52. Depending on the fitting algorithm, the amounts calculated for the rigid fraction determined by NMR can differ up to 10%. The combination of an Abragam function with two exponential functions (AEE) gives a good fit of the FID at temperatures between 40 and 100 °C. When increasing the temperature (T > 100 °C), this model results in a poorer fit. However, when taking into account the whole temperature range 40 − 140 °C by the AEE approach, the amount of the rigid fraction ($\%T_2^{\mathrm{rigid}}$) is closer to the crystallinity as determined by SAXS and DSC. When replacing the Abragam function with a Gaussian function in the above-mentioned combination of fitting functions, the measured amount of the rigid fraction is approximately 10 wt % higher. Therefore, by using the combination of AEE fit for the analysis of the NMR decay, an accurate determination of the phase composition of iPP samples can be performed.

The results obtained from both SPE and HEPS experiments, were combined in a single decay, which was fitted with a linear combination of one Abragam function and two exponential functions (Figure 1b)

$$A(t) = A(0)^{\mathrm{rigid}} \exp[-(t/2T_2^{\mathrm{rigid}})^2]\cdot[\sin(at)/at] + A(0)^{\mathrm{semirigid}} \exp[-(t/T_2^{\mathrm{semirigid}})] + A(0)^{\mathrm{soft}} \exp[-(t/T_2^{\mathrm{soft}})] \quad (1)$$

The parameter a is related to the second and fourth van Vleck moments. The transverse relaxation times (T_2), which are characteristic of different slopes in the magnetization decay curve, are related to the mobility in each fraction. The relative fractions of the relaxation components, $\{A(0)^k/[A(0)^{\mathrm{rigid}} + A(0)^{\mathrm{semirigid}} + A(0)^{\mathrm{soft}}]\} \times 100\%$, represent the relative amounts of hydrogen atoms (mass fractions) of iPP phases/fractions with different molecular mobility. Repeated experiments for the same sample indicated that the relative error of the extracted relaxation parameters was about 1%.

2.5.3. Spin-Diffusion NMR Experiments with Dipolar Filters. Spin-diffusion experiments with double-quantum (DQ) dipolar filter were performed to determine the thickness of the rigid and amorphous domains. Proton double-quantum buildup curves and spin-diffusion data were recorded at high- and low-magnetic fields using the pulse sequence $90°_x-\tau-90°_x-t_{\mathrm{DQ}}-90°_x-\tau-90°_x-t_{\mathrm{d}}-90°_x-$FID with the excitation time τ and the spin-diffusion time t_{d}. The evolution time of the DQ coherences is t_{DQ} which was taken as 5 μs in all experiments. The dipolar filter excites double-quantum coherences and selects mainly the magnetization of the rigid fraction at a short excitation time τ.[47,52] The optimum τ value in the DQ filter for selection the rigid fraction[54] was obtained from the DQ buildup curve. It shows one maximum for iPP (Figure 2) at short excitation times τ of approximately 10 μs. The efficiency of the filter is judged by the ^{1}H wide-line NMR spectra recorded at different excitation/reconversion times τ (Figure 3). These spectra allow us to choose the optimum filter time for selecting the magnetization of the rigid fraction. For short excitation/reconversion time τ, the DQ filtered spectra are doublets (Figure 3, parts a and b) which are related to the spin pairs of methylene groups having the strongest dipolar couplings. It should be further to mentioned that the doublet structure of the DQ-filtered spectra is due to the fact that at short excitation times, only the rigid polymer chains with dipolar tensor orientation around 0 and 90° are preferentially excited, while those orientated around the magic angle are suppressed. An interesting property of the DQ filter is that at long excitation times, only the signal from the most mobile chain fragments in the amorphous phase is selected (Figure 3d).

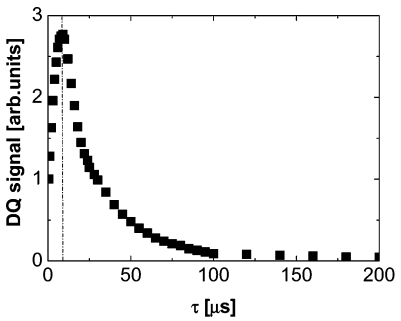

Figure 2. Proton DQ buildup curve for iPP at room temperature showing the dependence of the integral signal on the excitation time τ. The DQ buildup curve is measured with high-field NMR spectrometer. The maximum of the curve is observed at 10 μs that is marked by a dashed line.

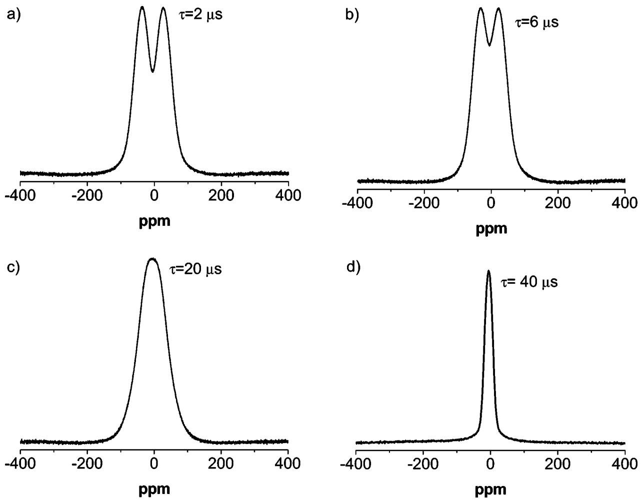

Figure 3. High-field proton wide-line NMR spectra of iPP at room-temperature recorded after different excitation/reconversion periods of the DQ dipolar filter: $\tau = 2$ μs (a), $\tau = 6$ μs (b), $\tau = 20$ μs (c), and $\tau = 40$ μs (d). The spin-diffusion time t_{d} was set to 5 μs.

The DQ filter shows high efficiency in selecting the magnetization of a particular iPP domain with distinct molecular mobility. The high selectivity of the DQ filter was also observed in T_2 relaxation experiments at low resonance frequency. For all experiments, the excitation/reconversion time of 10 μs and short spin-diffusion time t_{d} of 5 μs (Figure 4) were chosen to select the rigid iPP fraction in the spin-diffusion experiment, both at high- and low-proton resonance frequencies. The proton NMR spectra edited for different spin-diffusion times are shown in Figure 4.

Another dipolar filter used in this investigation explores the Goldman−Shen scheme.[50] The amorphous domains are selected by the pulse sequence $90°_x-\tau-90°_x-t_{\mathrm{d}}-90°_x-$FID with the filter time $\tau = 100$ μs and t_{d} being the spin-diffusion time. Both dipolar filters were employed in the present study to gain a higher confidence in determinations of the iPP morphology.

3. Results and Discussion

3.1. Crystallinity by DSC. Quantities like enthalpy, derived from heat capacity measurements, can provide important information about the physical state of the material. Heat capacity of iPP annealed for 10 h at 143 °C and iPP annealed for 10 h at 153 °C, is presented in Figure 5. Parts a and c of Figure 5 show heat capacity c_p and crystallinity W data for the first heating curve and the second heating/cooling curve, respectively. The observed differences between the first heating curve for nonannealed and iPP annealed for 10 h at 143and at 153 °C (Figure 5a) are due to the thermal treatment (thermal history) of the sample. For completion, heat capacity measure-

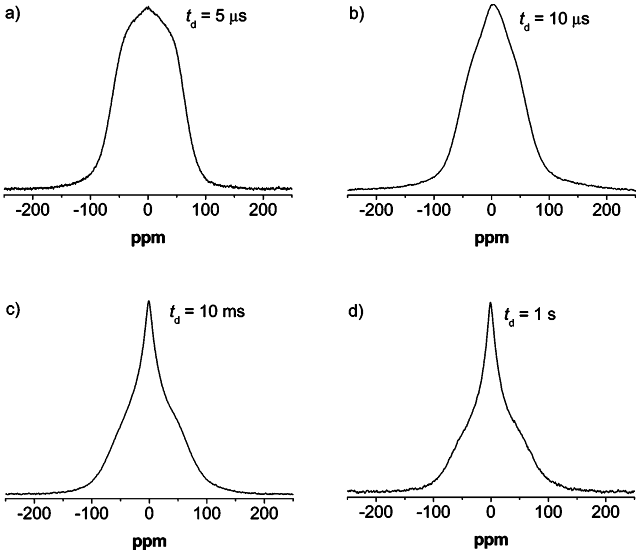

Figure 4. Proton wide-line NMR spectra of iPP at room temperature. The spectra were recorded using the spin-diffusion experiment with different spin-diffusion times: (a) $t_d = 0.005$ ms, (b) $t_d = 0.010$ ms, (c) $t_d = 10$ ms, and (d) $t_d = 1$ s and $\tau = 10$ μs.

ments of the cooling and second heating curve are presented as well in order to verify whether or not the thermal treatment modifies the polymer material. The thermal history of iPP is erased after the first heating scan and by keeping the polymer for 5 min in the molten state (200 °C) (Figure 5d).

Litvinov and Soliman showed that annealing of iPP gives rise to shoulders in the DSC thermograms.[55] In order to compare the annealed samples with nonannealed iPP, an offset temperature is defined in this study. The offset temperature corresponds to a drastic increase of the heat capacity due to melting of the polymer (see Figure 5b). Offset temperatures of 144 and 153 °C are observed for iPP annealed at 143 and 153 °C for 10 h, respectively. An apparent offset temperature of 134 °C (increase of C_p in comparison with the baseline) is observed for nonannealed iPP. The determined offset temperatures for the annealed samples correlate to the applied annealing temperatures. These observations are in agreement with the NMR data discussed below.

A complete heat capacity analysis is performed. The corresponding enthalpy, $H(t)$, can be derived in the usual way with calibration values. The extreme states in which the material can be found (100% crystalline and 100% amorphous) are referred to as reference states. These data are reported for a large number of polymers in the ATHAS Data Bank.[56]

Mathot has shown that the polymer can be regarded as consisting of regions having the same thermal properties as the reference states, and a simple two-phase model can be used in order to determine the enthalpy-based mass fraction crystallinity.[24] This means that no transition layers between the regions and no contributions from interfaces are taken into account for the analysis of DSC data in this study. We observed that the crystallinity of iPP, determined at 80 °C ($W_{80\ ^\circ\mathrm{C}}$), increases as expected with the annealing temperature: $W_{80\ ^\circ\mathrm{C}} = 50$ wt % for nonannealed iPP, 59 wt % for iPP annealed at 143 °C, and 61 wt % for iPP annealed at 153 °C, (Figure 6). After erasing the thermal history by melting, the crystallinity of iPP (Figure 6—second heating curve; the dashed, orange line) is somewhat higher than the crystallinity of nonannealed iPP (Figure 6—first heating curve; the straight, black line), but still lower than the crystallinity of both annealed iPP samples ($W_{80\ ^\circ\mathrm{C}} = 55$ wt % for the second heating curve). Thus, the crystallinity of iPP derived from the first heating curve shows a different thermal history than the one derived from the second heating curve (Figure 5d). The end of the melting behavior of the annealed samples is located at a higher temperature than that of the second heating curve (indicated in Figure 6 by the green arrow); this is expected when crystal thickening and crystal perfection occurs. NMR experiments also show improvement of crystal perfection upon annealing, as will be shown below. Crystal thickening is observed by NMR and TEM during annealing of iPP samples. Thus, results of NMR and TEM are in line with the heat capacity data.

3.2. Morphology of iPP by TEM. The transmission electron micrograph is used to determine the type of the morphology in the studied samples. A TEM image of the nonannealed iPP sample is shown in (Figure 7a). Stacked lamellar crystals separated by a thin amorphous layer can be observed. The annealed iPP samples at 143 and 153 °C for 10 h reveal a cross-hatched morphology (Figure 7b and 7c) consisting of radial and transverse lamellae. The thickness of the lamellae increases with increasing the annealing temperature.

3.3. Crystallinity and Morphology by SAXS. The crystallinity of both annealed and nonannealed iPP samples is determined by SAXS. Integration of the 2D-WAXD pattern over a pie-shaped area yielded the intensity profiles displayed in Figure 8a. In all cases, the sequence of the detected diffraction maxima is consistent with the monoclinic α-structure of polypropylene. The contributions arising from crystalline and noncrystalline components are extracted via peak fitting of the diffraction pattern (Figure 8b). The latter yielded the (X-ray) crystallinity which showed a 9% increase from a value of 0.49 ± 0.05 for the nonannealed system to 0.58 ± 0.05 for a sample annealed at 153 °C. These values are in good agreement with DSC crystallinity.

The SAXS patterns reveal well-defined interference maxima owing to a quasi-periodic arrangement of the crystalline domains. More details about the scattering and correlation functions are discussed in ref 52. The one-dimensional scattering intensities $I(q) \times q^2$ is shown in Figure 9, where $q = (2/\lambda) \times \sin\theta$, λ is the wavelength of the X-ray radiation and θ is the scattering angle. It follows from results in Figure 9 that annealing has a strong influence on the lamellae thickness. After annealing, the position of the interference maximum shifts toward lower scattering angles which indicates an increase of the effective long period. This is also reflected by the linear correlation functions, calculated from the scattering intensities (Figure 10). In this case, the position of the first side maximum indicates the changes in the value of the long period following different thermal histories. Moreover, the inner part of the correlation function provides insight into the thickness of one of the phases. However, it cannot be concluded directly whether or not the corresponding value reflects the thicknesses of the crystalline or the amorphous domains.

3.4. Solid-State NMR Study of Phase Composition, Molecular Mobility, and Domain Thickness. 3.4.1. Temperature Dependence of Phase Composition and Chain Mobility. A quantitative analysis of the FID and wide-line NMR spectra in terms of crystalline phase, semirigid phase, and soft fraction of the amorphous phase is performed at a temperature well above T_g. At these temperatures, the difference in molecular mobility of the iPP phases is higher, and therefore, the phase contrast is enhanced. However,, the temperature of the NMR experiment should not be too high, in order to avoid annealing and an associated change in the morphology.

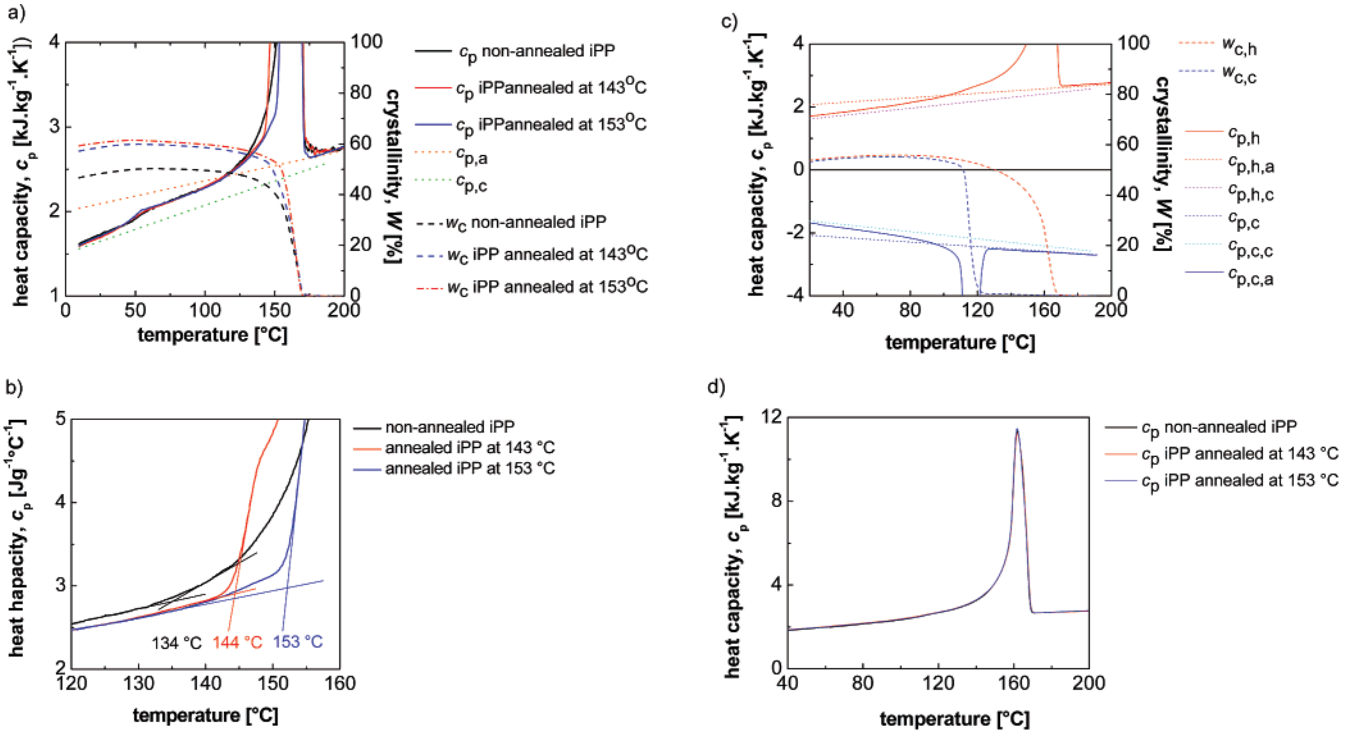

Figure 5. (a) Heat capacity (c_p) and crystallinity (W) data recorded during the first heating of nonannealed iPP (black solid and dashed lines), annealed at 143 °C iPP (red solid and dashed lines), and annealed at 153 °C iPP (blue solid and dashed lines). Annealing time is 10 h. The green and orange dotted lines represent the heat capacity for the crystalline ($c_{p,c}$) and amorphous ($c_{p,a}$) phases, respectively. (b) Heat capacity and onset of melting for nonannealed iPP (black line), annealed at 143 °C (red line) and annealed at 153 °C iPP (blue line), respectively. Annealing time is 10 h. (c) Heat capacity (solid lines) and crystallinity (dashed lines) recorded during the second heating ($c_{p,h,a}$ and $c_{p,h,c}$, $W_{c,h}$ cooling ($W_{c,c}$, $c_{p,c,a}$, and $c_{p,c,c}$) of iPP. Dotted lines represent the heat capacity for the amorphous and crystalline phase for second heating and cooling, respectively. (d) Heat capacity curves recorded for the second heating curves for nonannealed iPP (black line), iPP annealed at 143 °C (red line), and iPP annealed at 153 °C (blue line). Annealing time is 10 h.

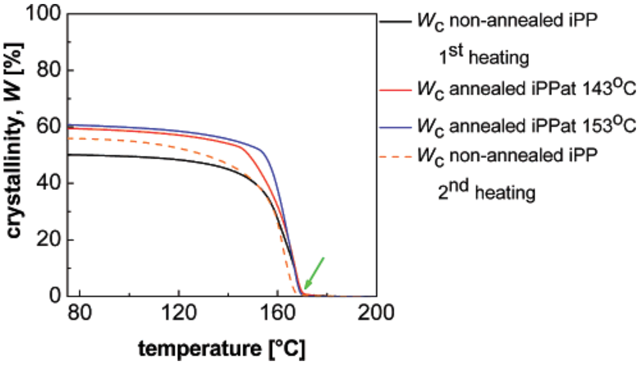

Figure 6. Crystallinity of iPP at the first heating curves (solid lines) of nonannealed iPP (black) and iPP annealed at 143 (red) and 153 °C (blue). Annealing time is 10 h. Crystallinity at second heating curve is shown by orange dashed line.

In order to find the optimum temperature to determine the phase composition, T_2 relaxation parameters and integral intensities of the spectral components of the ^{1}H wide-line NMR spectra are recorded as a function of temperature (Figure 11). At room temperature, a significant fraction of the soft phase is rigid, and contributes to both the intensity of the broad line of the NMR spectra, and the short T_2 relaxation component of the FID. At elevated temperature, the amount of the rigid fraction, which comprises the crystalline phase and the rigid fraction of the soft phase, slowly decreases. While the amount of the soft fraction increases under the same conditions, the amount of the semirigid fraction is almost constant in the temperature range from 70 to 100 °C (Figure 11). The data in Figure 12 show nearly constant values for T_2^{rigid} and $\Delta\nu_{1/2}^{\text{rigid}}$ with temperature increasing up to 100 °C, indicating that the molecular motion in the rigid fraction is almost unchanged. The small increases in T_2^{rigid} above 100 °C may be related to the motion in the crystalline phase—α relaxation process—which occurs prior to melting—and to the thermal expansion of crystal lattice.[57] In the temperature range from 40 to 60 °C, the transverse relaxation time of the semirigid and soft fractions increases largely, while $\Delta\nu^{\text{semirigid}}{}_{1/2}$, and $\Delta\nu^{\text{soft}}{}_{1/2}$ largely decrease (Figure 12). These changes are due to the high-frequency (ca. 10 kHz) manifestation of the glass transition of the amorphous phase. The temperature dependences of the T_2^{soft} and of $\Delta\nu_{1/2}^{\text{soft}}$ can be correlated by the relationship $\Delta\nu_{1/2}^{\text{soft}} \approx 1/\pi T_2$, valid for a Lorentzian line shape (Figure 12). In the temperature range from 100 to 140 °C, an increase in the T_2 relaxation time of the semirigid and soft fractions is due to partial melting of isotactic polypropylene. That reduces hindrances on chain mobility in the soft phase.

In conclusion, the temperature range from 70 to 100 °C appears to be suitable for accurate determination of the phase composition. In this temperature range, the difference in molecular mobility in different fractions of iPP is higher, and annealing can be avoided during the NMR experiment, as shown below. In the temperature range from 70 to 100 °C, the amount of the rigid fraction is largely independent of temperature, and its values is closed to that of the crystallinity measured by DSC and X-ray, as will be discussed below.

3.4.2. The Effect of Annealing Temperature and Annealing Time on the Phase Composition and Molecular Mobility. To determine the temperature at which annealing causes changes in the morphology, two different types of annealing studies were performed. The annealing was studied at isothermal conditions in the temperature range from 70 to 130 °C in real time. The data are recorded over each hour during 30 h. No annealing effects are detected by NMR for iPP samples exposed to 70,

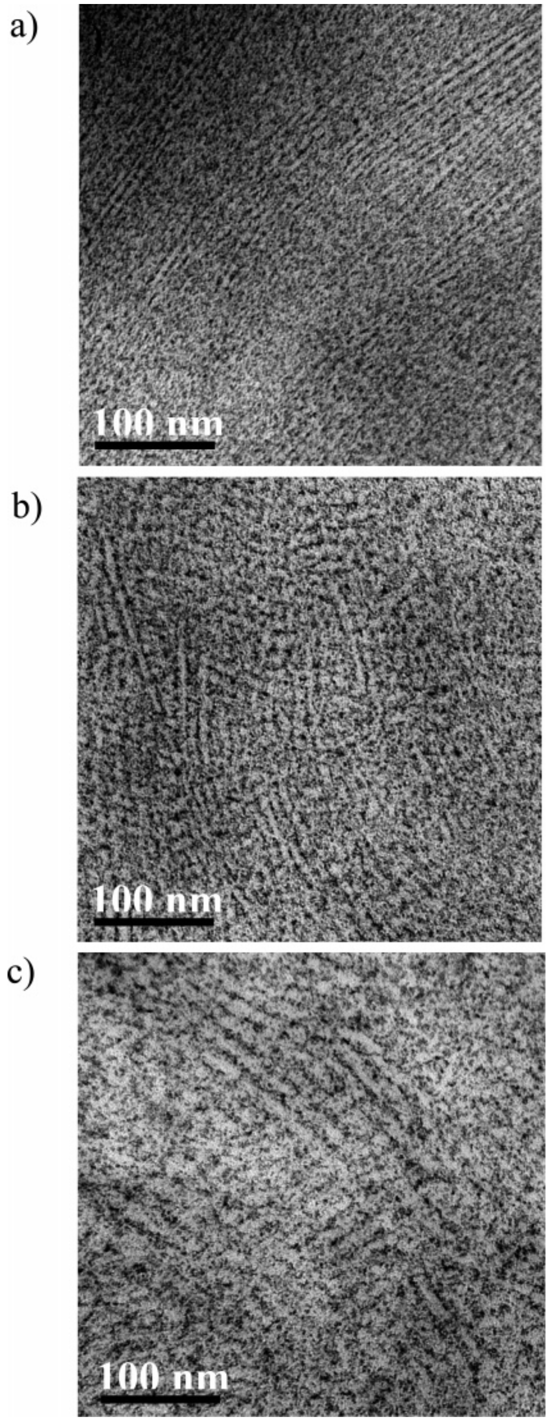

Figure 7. TEM image for nonannealed iPP (a) and iPP annealed at 143 (b) and 153 °C (c). Annealing time is 10 h. The scales of the images are shown in the figures.

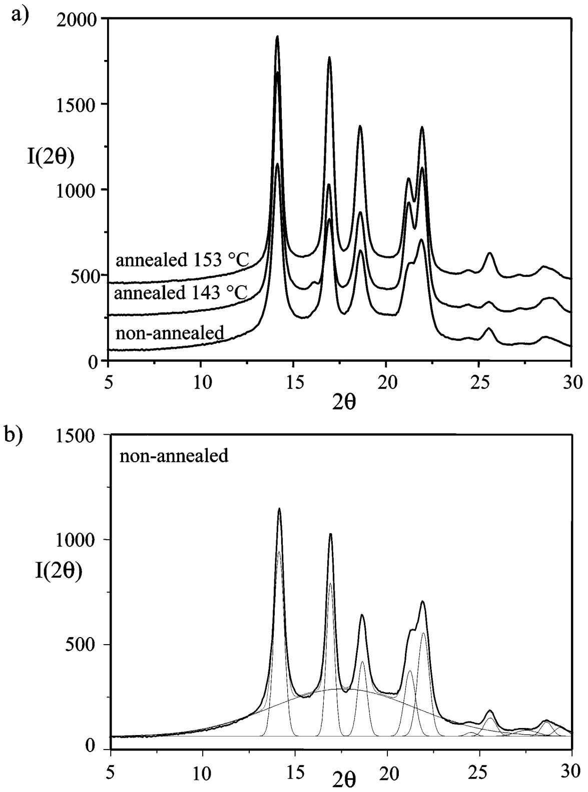

Figure 8. (a) One-dimensional WAXD intensities obtained via integration of two-dimensional WAXD patterns for nonannealed iPP, and iPP annealed at 143 and 153 °C for 10 h. (b) deconvolution of WAXD pattern for crystalline and amorphous phases for nonannealed iPP.

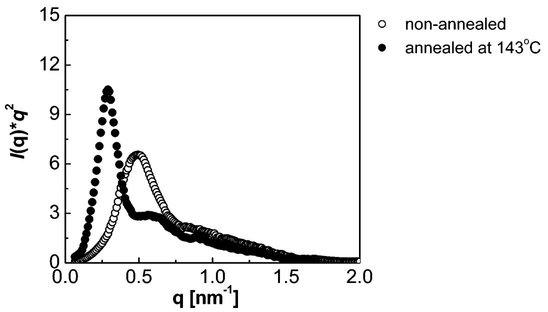

Figure 9. One-dimensional SAXS intensity $I(q) = I(q) \times q^2$ recorded for nonannealed iPP and iPP annealed for 10 h at 143 °C.

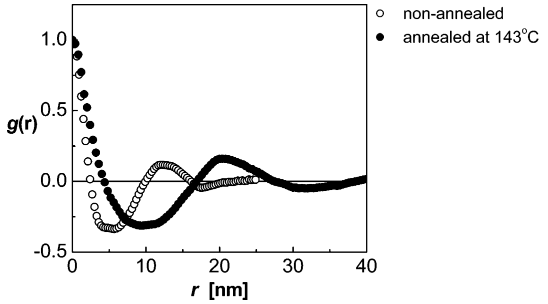

Figure 10. Normalized linear correlation function $\gamma(r)$ revealing an increase in the long period and phase dimensions due to annealing at 134, 143, and 153 °C for 10 h.

90, and 110 °C for 30 h. In the temperature range from 110 to 130 °C, small changes in the molecular mobility and the phase composition were observed over a time of 500 h. Annealing at 130 °C for 500 h causes $\approx$ 5 wt% increase in the amount of the rigid fraction at the expense of the soft phase. The amount of the semirigid phase remains almost constant (Figure 13a). Annealing caused changes in T_2 values (Figure 13b). Figure 13b show that the molecular mobility in the crystalline phase of iPP is hardly affected by annealing at 130 °C, whereas the molecular mobility of the semirigid fraction decreases and the molecular mobility in the soft fraction increases during the annealing. From the above results, we can conclude that exposure of iPP to temperatures between 100 and 130 °C influences the NMR results, due to the annealing of the samples during NMR experiments. These experiments are used to determine the maximum temperature at which no annealing occurs.

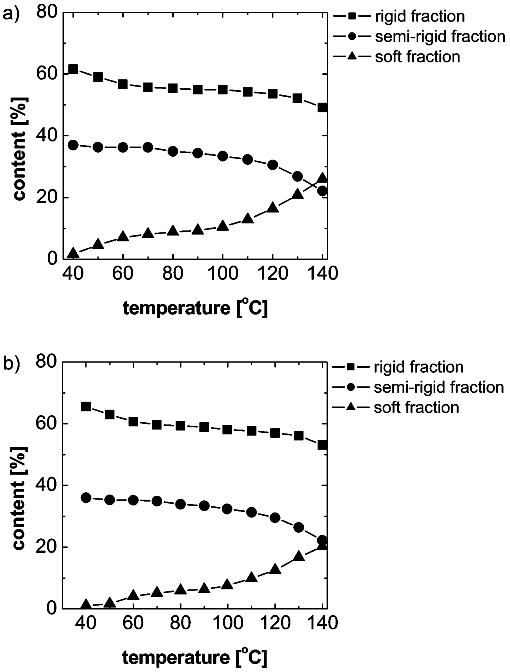

Figure 11. Temperature dependence of the amounts of rigid (%T_2^{rigid}), semirigid (%$T_2^{semirigid}$), and soft (%T_2^{soft}) fractions of nonannealed iPP as measured with low-field (a) and at high-field (b) NMR spectrometers.

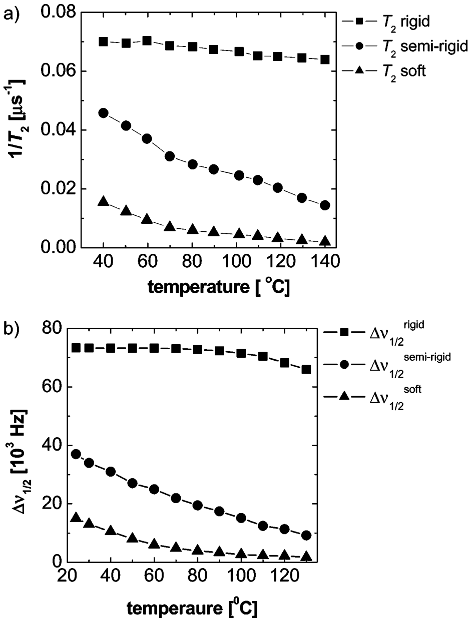

Figure 12. Temperature dependence of the ^{1}H 1/T_2 relaxation rates (a) and line-width $\Delta\nu_{1/2}$ (b) for nonannealed iPP. The assignment of the parameters to the rigid, semirigid, and soft fractions of iPP is shown in the figure.

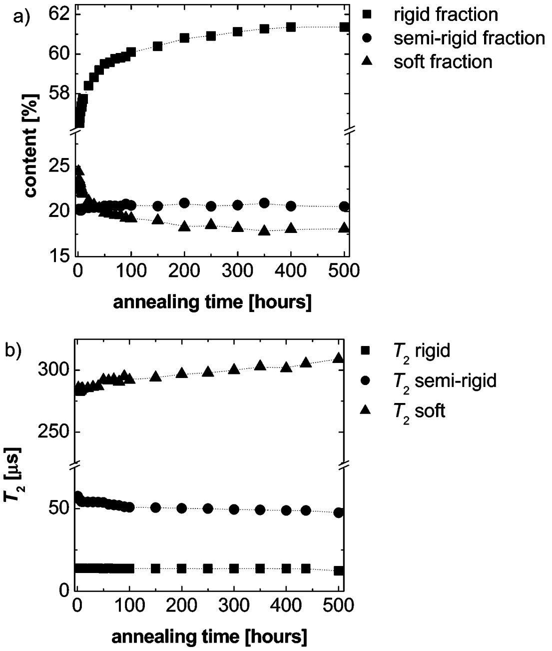

Figure 13. (a) Amounts of rigid phase (% T_2^{rigid}), semirigid interface (% $T_2^{semirigid}$), and soft fractions (% T_2^{soft}) of iPP as a function of the annealing time at 130 °C. (b) Effect of the annealing on molecular mobility, as determined by the T_2 relaxation time for the different fractions of iPP. Larger amplitude and/or frequency of molecular motions lead to longer T_2 value. The relaxation characteristics were determined by the analysis of FID, (rigid and semirigid fractions), and Hahn-echo (soft fraction), as described in experimental section. The experiments were performed with low-field NMR spectrometer.

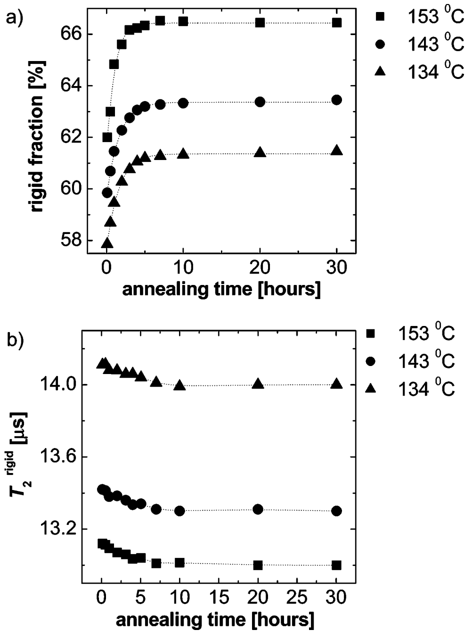

Figure 14. Effect of annealing time and annealing temperature on (a) the amount of the rigid fraction (% T_2^{rigid}), and (b) ^{1}H relaxation time (T_2^{rigid}) of this fraction of iPP.

The effects of the annealing time and the annealing temperature on the phase composition and molecular mobility were studied for iPP samples annealed at 134, 143, and 153 °C. The annealing times are taken in the range from 15 min to 30 h. After annealing at the indicated temperatures, the NMR experiments were performed at 70 °C. A fast increase in the amount of the rigid fraction is observed during the first 5 h of annealing at 134, 143, and 153 °C (Figure 14a). The amount of the rigid fraction increases by a few weight percent at the expense of the soft fraction. The amount of the semirigid fractions remains almost constant. It is also observed that molecular mobility in rigid and semirigid fractions of iPP decreases, while the molecular mobility of the soft fraction increases during the annealing. This increase is due to the better organized morphology of iPP during annealing. This is shown by the decrease in the T_2 values for the rigid fraction (T_2^{rigid}) (Figure 14b), the semirigid fraction ($T_2^{semirigid}$), and increase in the T_2 values for soft fraction (T_2^{soft}). The observed changes during annealing can take place for the following reasons: formation of thin lamellae

Table 1. Amounts of Rigid Fraction/Crystallinity Obtained by NMR, SAXS, and DSC for Nonannealed and Annealed iPP Samples for 10 h

	NMR 70 °C (wt %)			SAXS (vol %)		DSC (wt %)	
	rigid	semirigid	soft	crystalline	amorphous	crystalline	amorphous
nonannealed	56	36	8	51	49	51	49
annealed at 143 °C	67	26	7	55	45	59	41
annealed at 153 °C	70	24	6	58	42	61	39

between the primary lamellae, lamella thickening, and improvement of the ordering in different phases.[20,58]

3.4.3. Comparison of the Amounts of Rigid Fraction/Crystallinity Obtained by NMR, SAXS, and DSC. It can be anticipated that the crystallinity values determined by different methods for the same sample are not exactly the same. By comparing the results of different methods, the complex morphology of semicrystalline polymers can be understood better. The difference between the amounts of the rigid fraction that is obtained by the NMR experiment at 70 °C and the degree of crystallinity obtained from DSC and SAXS for both annealed and nonannealed iPP does not exceed 10% (Table 1). All methods used show increase in the amount of the rigid fraction/degree of crystallinity with increasing annealing temperature.

There are several reasons for the apparent differences between the results obtained by NMR, DSC, and SAXS. They could be attributed to the following: (i) The discrimination between the rigid and soft fractions is made based on different characteristic parameters, such as the enthalpy of melting (measured by DSC), the mobility (measured by NMR), and the long range periodicity (measured by SAXS). (ii) The complex morphology of semicrystalline polymers requires various assumptions for the analysis of data recorded by different methods. For example, a parameter influencing the NMR crystallinity is the temperature at which the samples are analyzed. At 70 °C, a small fraction of the soft phase can be immobilized at the time scale of the NMR experiment, and this immobilized fraction contributes to the intensity of the broad line of the NMR spectra and also to the T_2^{rigid} relaxation component of the FID. This can be concluded by comparing the amounts of the whole rigid fraction at 70 °C (56 wt %) with the crystallinity determined by SAXS and DSC (51 ± 5 wt %). (iii) The two-phase model normally used to describe the morphology of semicrystalline polymer does not take into account the presence of the semirigid fraction (interface). This can be detected by either as a rigid/ordered or soft/disordered fraction,[39] depending on the method used. Despite the fact that the amount of the rigid fraction is determined using the three-phase model for the analysis of the NMR data, the NMR crystallinity exceeds by 5−10 wt % that which is obtained by DSC and SAXS, using the classical two-phase model. We suggest that small crystals between lamellae, which contribute to the amount of the rigid fraction, are not detected by SAXS and DSC due to the low electron density and low enthalpy of melting compared to that of the well-ordered large lamellae.

3.4.4. Temperature Dependence of ^{1}H Spin Diffusivities. An accurate analysis of the thickness of domains by NMR spin-diffusion experiments requires three steps. These are as follows: (i) an optimization of a dipolar filter to obtain the highest selectivity to the different phases (see section 2.5.3), (ii) knowledge of the spin-diffusion coefficients for modeling the experimental data, and (iii) proper choice of a model that describes the morphology of the material studied (see section 3.4.5). The values of the spin-diffusion coefficients, which are required for the determination of the domain thickness by NMR spin-diffusion experiments, should change with increasing temperature due to an increase in molecular mobility and interchain distances.[52] Therefore, the spin-diffusion coefficients should be determined at different temperatures.

The values of the spin-diffusion coefficients D_{f} (f = r, a) for the rigid (crystalline) and amorphous fractions can be determined by approximating, the NMR line shapes of the rigid and the amorphous fractions by Gaussian and Lorentzian functions, respectively.[51] Since the reliable fit of FID from the spin-diffusion experiments was possible with two components, which is due to the small amount of the soft fraction, more simplified two-phase model is used for determination of the thickness of crystalline and amorphous domains. In this case, the thickness of the amorphous domains, correspond to the thickness of the semirigid and soft domains. The spin-diffusion coefficients can be related to the second van Vleck moment of the NMR absorption lines, which, in turn, are related to the full line width $\Delta\nu_{1/2}$ at half-height. The temperature dependences of $\Delta\nu_{1/2}$ were determined at each temperature by spectral deconvolution as shown in Figure 1a. at one temperature. Hence the spin diffusivity for the rigid (D_{r}) and amorphous (D_{a}) fractions are expressed as follows:

$$D_{\mathrm{r}} \approx \frac{1}{12}\sqrt{\frac{\pi}{2\ln 2}}\,\langle r^2\rangle \Delta\nu_{1/2}^{\ \mathrm{rigid}} \tag{2}$$

and

$$D_{\mathrm{a}} \approx \frac{1}{6}\langle r^2\rangle [\alpha \Delta\nu_{1/2}^{\ \mathrm{amorphous}}]^{1/2} \tag{3}$$

where $\langle r^2\rangle$ is the mean square distance between the nearest spins, $\Delta\nu_{1/2}^{\mathrm{a}}$ is the line width of the semirigid and soft fractions, and α is a cutoff parameter for the Lorentzian line shape.[51] The following assumption is made for calculating $\langle r^2\rangle$. Since the strength of the dipolar interactions largely decreases with increasing proton−proton distance, only the nearest neighbor proton−proton intrachain distances smaller than 0.3 nm are taken into account, and the interchain interactions are neglected. The discover program (version 2004.1) was used for calculating the proton−proton distances. The estimated weight mean square of these distances $\langle r^2\rangle$ is approximately 0.08 nm^2.

The calculated spin-diffusion coefficients are plotted as a function of temperature in Figure 15a. The values of the spin-diffusion coefficients decrease with increasing temperature, due to both an increase in the amplitude and the frequency of the chain motion in each fraction of iPP. The increase in the chain mobility causes more efficient averaging of the proton dipole−dipole interactions, and reduces the efficiency of the spin-diffusion.

The temperature dependence of the spin diffusivity in different fractions of iPP is difficult to predict quantitatively, due to the complex origin of the chain motion and multispin interactions. Nevertheless, a semiquantitative approach can be presented based on the arguments provided in ref 59. In the presence of motions of the spins, the theory of the NMR line width predicts that $\Delta\nu_{1/2} \approx M_{2,\mathrm{rigid}}\tau_{\mathrm{c}}$, where $M_{2,\mathrm{rigid}}$ is the second van Vleck moment for a rigid polymer, and τ_{c} is the correlation time for the chain motions. From eq 3 and the above relationship, one obtains: $D_{\mathrm{a}} \propto (\tau_{\mathrm{c}})^{1/2}$. The temperature dependence of the

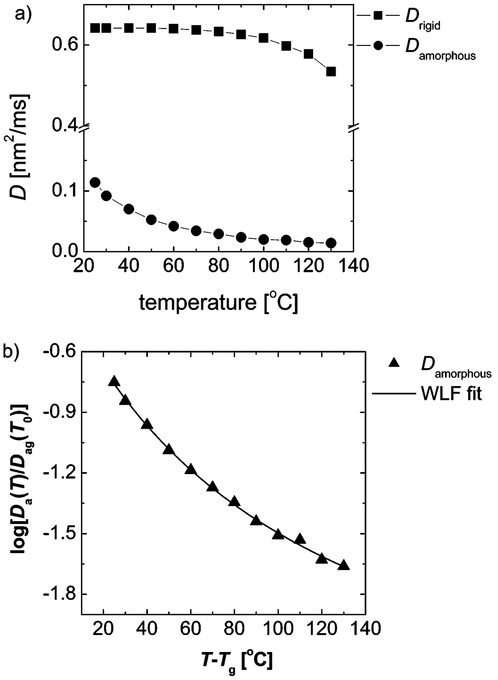

Figure 15. (a) Temperature dependence of the spin-diffusion coefficient for the rigid D_r and amorphous D_a fractions of iPP. (b) Dependence of $\log[D_a(T)/D_{ag}(T_0)]$ on temperature. The line shows the fit of the dependence with eq 5.

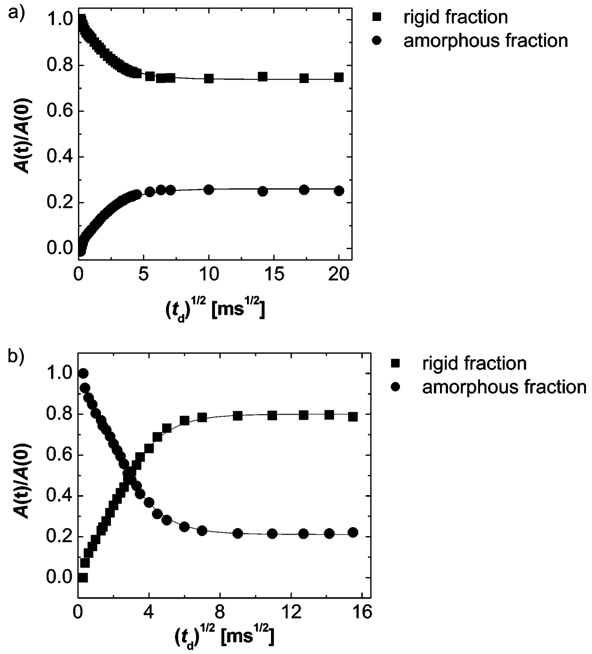

Figure 16. Proton spin-diffusion decay and buildup curves for the rigid (■) and amorphous (●) fractions of nonannealed iPP recorded using the DQ (a) and GS (b) dipolar filters. These filters select the magnetization of the rigid and amorphous fractions of iPP, respectively. The time-domain data were recorded at 70 °C with low-field NMR spectrometer and fitted with one Abragam function and one exponential function. The filter time for the GS was set to 100 μs. The solid lines represent the best fit for the 1D solutions of the spin-diffusion data for the two-phase morphology.

correlation time in amorphous polymers can be approximated by the Williams−Landel−Ferry (WLF) equation (see ref 57), i.e.

$$\tau_c(T) = \tau_c(T_g) \exp\left[\frac{-C_1(T - T_g)}{T - (T_g - C_2)}\right] \tag{4}$$

where T_g is the glass transition temperature and C_1 and C_2 are the WLF coefficients.

Using the above equation, the temperature dependence of the spin diffusivity D_a of the amorphous fraction of iPP can be described by the following equation.

$$D_a(T) = D_{ag} \exp\left[\frac{-\left(\frac{C_1}{2}\right)(T - T_g)}{T - (T_g - C_2)}\right] \tag{5}$$

where D_{ag} is the spin-diffusion coefficient at temperatureT_g. The spin-diffusion coefficient of the rigid fraction at 25 °C is taken as $D_{a0} \approx D_{ag}$ (see Figure 15a). A least-squares fit of the dependence in Figure 15b provides the following values of the WLF parameters: $C_1 = 10$, $C_2 = 57$ K, and $T_g = 273$ K. These values are in the range of typical WLF coefficients that describe dynamic mechanical and dielectric data for amorphous polymers, namely $C_1 \approx 16$ and $C_2 = 25-104$ K.[60] The observed differences could be because the WLF function is originally proposed to describe the temperature dependence of the viscosity. An increase in the amplitude and the length scale of the chain motion with increasing temperature could affect the spin-diffusion coefficients and mechanical data in a slightly different way.

3.4.5. Morphology of iPP by ^{1}H Spin-Diffusion. The ability of NMR spin-diffusion experiments to provide self-consistent information on the dimensionality of the diffusion process was discussed in ref 51. Proton spectra recorded at 70 °C with the DQ filter after different diffusion times are shown in Figure 4. The flow of longitudinal magnetization from the rigid domains to the amorphous domains is observed with increasing diffusion time, causing an increase in the intensity of the narrow line at the expense of the broad line. The time-dependent integral of the spin-diffusion spectra intensities reach their equilibrium values for iPP samples in about 70 ms. In a good approximation, the spin-diffusion DQ edited ^{1}H NMR spectra can be decomposed into two components. The two-component analysis is use to establish the average thickness of rigid (crystalline) and amorphous domains. It can be shown that the solutions of the spin-diffusion equations for different morphologies exhibit different sensitivities to the dimensionality of the process, as a result of different surface/volume ratio (interface area) for a given source volume. The information about the dimensionality of the spin-diffusion process can be obtained using the following equations:[61]

$$\begin{aligned} \frac{rE}{p} &= 1, \quad \text{1D case} \\ \frac{rE}{p(2+p)} &= 1, \quad \text{2D case} \\ \frac{rE}{(1+p)^3 - 1} &= 1, \quad \text{3D case} \end{aligned} \tag{6}$$

where $r = \rho_r/\rho_a$ and $E = M_{a,eq}/M_{r,eq}$. The equilibrium magnetizations for the amorphous and rigid domains are denoted as $M_{a,eq}$ and $M_{R,eq}$, respectively. The ratio between the domain thicknesses d_a and d_r is denoted by $p = d_a/d_r$. In the two-phase approximation, the r and E values for nonannealed iPP samples are obtained as 1.11 and 0.25, respectively. These values are established independently of the spin-diffusion process. The spin-diffusion decay and buildup curves shown in Figure 16a

Table 2. Long Period (L_p) and the Thicknesses of Rigid (d_c) and Amorphous (d_a) Domains, at 70 °C, for Nonannealed iPP Samples Obtained by NMR Spin-Diffusion Experiments for 1D, 2D, and 3D Morphological Models

model	d_r (nm)	d_a (nm)	L_p (nm)
1D	10	2.5	12.5
2D	15.4	3	18.4
3D	21	3.5	24.5

Table 3. Spin-Diffusion Dimensionality, As Determined by Eq 6, for Nonannealed iPP

dimensionality	dimensionality ratio	values of the dimensionality ratio
1D	rE/p	1.2
2D	$rE/[p(2+p)]$	0.68
3D	$rE/[(1+p)^3-1]$	0.52

are fitted with the solutions of the spin-diffusion equations for 1D, 2D, and 3D morphologies.[47,62] For each spin-diffusion dimensionality, the values of d_a and d_r are established from the best fit (Table 2). These values are used to estimate the ratio p. The estimated dimensionality ratios (eq 6) are near unity which corresponds to the 1D lamellae morphology (Table 3). The values of the proton densities for the different phases of iPP, which are required for the calculation of domain thickness, are determined from the densities of the crystalline and amorphous phases of iPP, i.e., $\rho_c = 0.94$ g/cm^3 and $\rho_a = 0.84$ g/cm^3.[63] No correction of the spin-diffusion data due to the longitudinal relaxation effect, has been performed, because the spin-diffusion process is nearly completed at the longest mixing time of $t_d =$ 70 ms. This time is significantly shorter than $T_1 = 120$ ms. Moreover, the absolute values of relative fractions instead of the absolute values of the signal intensities, compensate to a large extend for the effect of T_1 relaxation in the present case.

3.4.6. Comparison of the Domain Thicknesses Measured by the DQ and the Goldman—Shen Dipolar Filters. The confidence in the values of the domain thickness and the effective dimensionality of the ^{1}H spin-diffusion process can both be enhanced if the experiments are performed on the same iPP sample using different dipolar filters. In this case, we employed DQ and Goldman−Shen (GS) filters. These dipolar filters select the initial magnetization in the rigid and amorphous domains, respectively.

The measurements of ^{1}H spin diffusion using both dipolar filters were performed on the nonannealed iPP sample at 70 °C with low-field NMR. The spin-diffusion buildup and decay spin-diffusion curves are shown in Figure 16. From these data, it is evident that the spin-diffusion process reaches the quasi-equilibrium state after diffusion time on the order of td ≈ 70 ms for both filters. Moreover, for the DQ filter, the quasi-equilibrium of the relative magnetization for the rigid and amorphous phases equals 0.73 and 0.27, respectively. In the case of GS dipolar filter, the corresponding phase fractions are 0.79 and 0.21. In the limit of experimental errors, these two results prove that both dipolar filters provide similar values of domain thickness. Small differences exist because the efficiency of the dipolar filters in selecting the magnetization just from one domain is not 100%, and the shape of the relaxation components biases the accuracy of the FID deconvolution procedure.

Table 4. Thicknesses of the Rigid (d_r) and Amorphous (d_a) Domains of Nonannealed iPP Measured at 70 °C Using Spin-Diffusion Experiments with Double-Quantum (DQ) and Goldman−Shen (GS) Dipolar Filters (Figure 16)

dipolar filter	d_r [nm]	d_a [nm]
DQ	10	2.5
GS	9	3

Table 5. Long Period (L_p) and the Thickness of Rigid (d_c) and Amorphous (d_a) Domains, at Different Temperatures for Nonannealed iPP Samples.

thickness	$T = 70$ °C	$T = 100$ °C	$T = 130$ °C
d_r (nm)	10 (10.5)	11.4 (12)	12 (12.5)
d_a (nm)	2.5 (2.1)	3.5 (3)	7 (7)
L_p (nm)	12.5 (12.6)	14.9 (15)	19 (19.5)

[a] The domain thicknesses were determined from ^{1}H spin-diffusion experiments with a DQ filter measured at low- and high fields (in parentheses) NMR spectrometers, respectively.

Table 6. Long Period[a] (nm) of Nonannealed iPP and iPP That Was Annealed for 10 h at 143 and 153 °C As Determined by NMR and SAXS

	nonannealed	annealed at 143 °C	annealed at 153 °C
NMR (70 °C)	12.5	19.9	21.3
SAXS data	12.9	21	21.8
SAXS, linear correlation function	12.5	20	21

[a] The average errors are on the order of 15%

The thickness of the rigid (d_r) and amorphous (d_a) domains are determined from fits of the spin-diffusion data (Figure 16) with the 1D solutions of the spin-diffusion equations. The approximation of two phases should not have a large effect on the extracted domain thicknesses, taking into account the small amount ≈ 4 wt % of the soft fraction. The time dependence of the analytical spin-diffusion signals for the GS filter can be obtained from those of the DQ filter, by interchanging the indices r and a of the quantities present in the spin-diffusion solutions. The domain thicknesses obtained by fits of the spin-diffusion data of Figure 16 are given in Table 4. The time domain data are fitted with a combination of one Gaussian and one exponential function, and with a combination of one Abragam and one exponential function. The domain thickness with values closest to that measured by SAXS, is that obtained from the free induction decay deconvoluted with the sum of one Abragam and one exponential function. Moreover, both dipolar filters provide a volume ratio of the rigid and amorphous domains that is close to the mass fraction of these phases, as determined from the FID at different temperatures, i.e., $d_r/d_a \approx 2 \div 5$ and $\%T_2^{\text{rigid}}/\%T_2^{\text{amorphous}} \approx 3-4.8$. These results provide additional proof of validity of the method for domain thickness determination, as well as the type of morphology. The thicknesses of the iPP domains determined by time-domain and frequency domain spin-diffusion experiments are in good agreement (Table 5).

3.4.7. The Temperature Dependence of the Domain Thickness. In order to estimate the domain thickness of the rigid and amorphous fractions, the spin-diffusion experiment was performed for nonannealed iPP samples at three different temperatures 70, 100, and 130 °C. The thickness of rigid and amorphous domains as well as the long period increases with increasing the temperature (Table 5). These changes can be explained by melting of the small disordered crystals upon increasing temperature and lamellae thickening.

3.4.8. The Effect of Annealing Temperature and Annealing Time on the Domain Thickness in iPP Samples. The long period, L_p, and the thickness of the rigid, d_r, and amorphous, d_a, domains, was studied as a function of annealing temperature and annealing time. The spin-diffusion experiments were

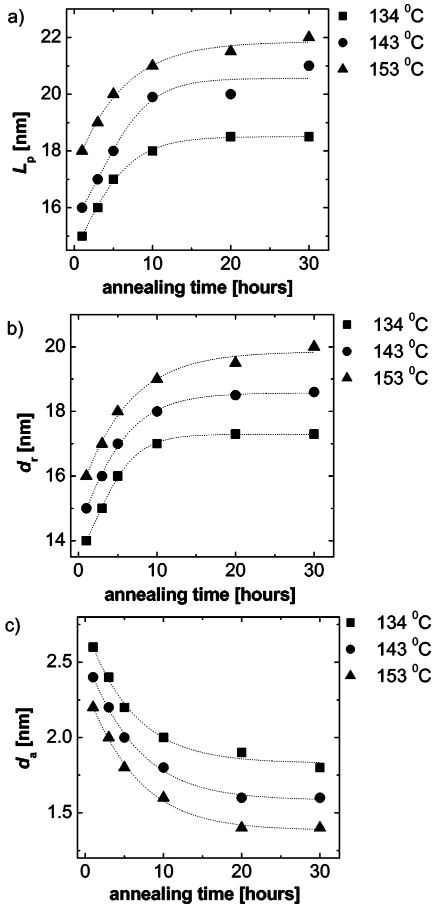

Figure 17. Changes of the (a) long period L_p, (b) thickness of rigid domains d_r, and (c) thickness of amorphous domain d_a of iPP as a function of annealing temperature and annealing time. The domain thicknesses were determined from ^{1}H spin diffusion experiments exploring a DQ filter. The experiments were performed with a low-field NMR spectrometer.

performed at 70 °C for the iPP samples, annealed at three different temperatures, and different annealing times. The values of the long period before and after annealing, determined by NMR spin-diffusion experiment and SAXS, are in a good agreement (Table 6). Figure 17 shows the changes of L_p, d_c, and d_a during the annealing. A rapid initial increase in the long period and in the thickness of the rigid domains is observed for the iPP samples during first 10 h of annealing (Figure 17ab). The rapid increase in the crystal thickness with annealing is confirmed by the increase in the crystallinity (Figure 14a, Table 1, and Table 6). For long annealing times, ranging between 10 − 30 h, the L_p and d_c do not seem to change significantly, showing a stabilization of iPP morphology (Figure 17ab).[64] The thickness of the amorphous domains slightly decreases with increasing the annealing temperature and annealing time (Figure 17c). Chain dynamics and thermodynamic factors play an important role in the annealing. The growth of lamellae involves translational motion of the polymer chains.[67] Faster chain diffusion through iPP crystals, and higher chain mobility in the amorphous phase upon increasing the temperature, facilitate the structural reorganization toward thermodynamically more stable thicker crystals.[65,68] Previous studies have also shown that the annealing of iPP samples at sufficiently high temperature increases the thickness of the lamellae.[64,66,67]

3.4.9. Crystalline Domains Thickening During Annealing. The spin diffusion NMR experiment measures the smallest dimension of the crystalline regions, i.e., the thickness of the crystal. This quantity changes during annealing, and this process is known as crystal thickening.

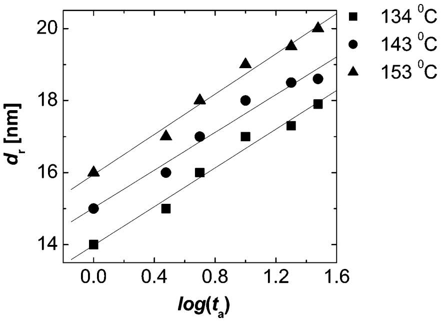

Figure 18. Change of the thickness of the rigid domains d_r upon the annealing time t_a at three different annealing temperatures. The straight lines are a least-squares fit of the data using eq 8.

The polymer crystals when annealed isothermally are thermodynamically metastable since they are formed with high surface-to-volume ratios. The thickening can be considered as a process of going from a state of higher to one of low free energy. For thin polymer crystals, a thermodynamics force capable of driving the thickening phenomena arises from the unequal free energies of the fold and lateral surfaces. This process is an irreversible thermodynamic process that can be described by the nonlinear differential equation[68]

$$\frac{\mathrm{d}y}{\mathrm{d}t} = \frac{2}{\tau_t}\left(\frac{1 - y^{3/2}}{y}\right) \qquad (7)$$

where $y = d_r/d_{r0}$, d_{r0} is the equilibrium thickness of the crystal at the end of the annealing, $\tau_t = kd_{r0}{}^2$and k is a proportionality constant. The above equation describes the changes in the crystal thickness from the values at the beginning of the annealing to d_{r0}. The temperature dependence of the thickening rate should enter the theory through k, or equivalently τ_t. When τ_t is assumed to be independent of d_r, the above equation can be integrated analytically, and the transverse crystal thickness d_r exhibits a sigmoidal shape as a function of $\log(t_a/\tau_t)$.[68−73] At the intermediate values oflog (t_a/τ_t), the crystal thickness increases approximately linearly with a higher rate at higher temperatures. Therefore, in the intermediate range of the annealing time t_a, the rigid domain thickness d_r measured by spin-diffusion can be described by the relationship

$$d_r \approx d_r(\tau_t) + B\log(t_a/\tau_t) \qquad (8)$$

For an annealing time $t_a = \tau_t$ we get from the above equation $d_r \approx d_r(\tau_t)$. When $t_a = 10\tau_t$, we get the significance of the constant B, i.e., $B \approx d_r(10\tau_t) - d_r(\tau_t)$.

The dependence of the rigid domain thickness for iPP annealed is shown in Figure 18 at three different temperatures as a function oflog (t_a). At all the annealing temperatures, the data can be fitted with a straight line in agreement with eq 8. Therefore, the process of crystal thickening upon annealing for iPP can be described in the linear approximation regime by eq 8 that can be derived from eq 7.[68,71] A strong temperature dependence of the thickening rate is not detected (cf. Figure 18) probably due to the limited range of annealing temperatures. Nevertheless, a very small increase in the slop of the fit line at annealing temperature of 153 °C is evident in Figure 18. Moreover, the thickening rate is primarily a function of undercooling $\Delta T = T^\circ_m - T$, where T°_m is the equilibrium melting point of the crystal (about 182 °C for iPP[74]), rather than the absolute temperature T.

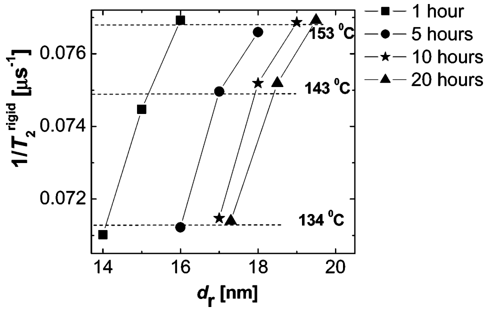

Figure 19. Correlation between the ^{1}H transverse magnetization relaxation rate ($1/T_2^s$) of the rigid domains and the thickness of these domains for iPP that was annealed at 134, 143, and 153 °C for 1, 5, 10, and 20 h. The NMR measurements were performed at 70 °C using low-field NMR spectrometer. The lines are a guide for the eye.

3.5. Correlation between ^{1}H Transverse Relaxation Rate and the Domain Thickness of the Crystalline Domains. The microscopic properties of iPP are represented by several parameters that describe the polymer chain dynamics. These dynamics correlate with the local structure in the nanoscale range and are revealed inter alia by the ^{1}H transverse magnetization relaxation rates. The morphology and domain thickness characterize the materials on the mesoscopic scale, i.e., on the scale of tenth or hundreds of nanometers.

The values of the ^{1}H effective transverse magnetization relaxation rate ($1/T_2^s$) for the rigid domain is related to the residual second van Vleck moment $\langle M_2\rangle$, i.e., $1/T_2^s \propto \langle M_2\rangle$. This is evident from the fact that the free induction decay $G(t)$ of the rigid domains in the short time domain is described in a good approximation by the Gauss function $G(t) \propto \exp(-\langle M_2\rangle/2\ t^2)$. An effective short relaxation time T_2^s can be introduced to describe this decay by the function $G(t) \propto \exp[-(t/T_2^s)^2]$, and hence we obtain

$$\frac{1}{T_2^{\,s}} = \left(\frac{\langle M_2\rangle}{2}\right)^{1/2} \tag{9}$$

Consequently, faster transverse relaxation rates correspond to larger values of $\langle M_2\rangle$ due to larger strength of the dipolar couplings. This is the case of slower chain motions, and increased interchain dipolar interactions due to denser chain packing and/or better crystals organization.

A phenomenological attempt to correlate $1/T_2^s$ and d_r quantities for different annealing temperatures and annealing times is shown in Figure 19. The transverse magnetization relaxation and spin-diffusion measurements were made at the same temperature of 70 °C. Therefore, the changes in the values of $1/T_2^s$ are due to the crystal thickening and perfection of crystalline order during annealing. The theory of polymer annealing[68,71−73] predicts that for a given annealing temperature the crystalline domain thickness increases linearly with $\log(t_a)$ (see eq 8), where t_a is the annealing time. This is evident from the values of d_r measured as a function of t_a at different annealing temperatures (Figure 19). Only small changes in the values of $1/T_2^s$ are detected at each annealing temperature as a function of annealing time. This parameter increases slightly with annealing time due to an increase in the density (perfection) of the crystalline regions during annealing.[68] This leads to an increase in $1/T_2^s$, due to an increase in the ^{1}H dipolar couplings, and consequently in $\langle M_2\rangle$. Higher annealing temperatures lead to more perfect and better-packed crystals in which fast small-angle fluctuations are reduced. Moreover, we note that this major effect occurs rapidly, and only minor further changes are observed during the course of annealing. This shows that there is no simple correlation between $1/T_2^s$ and crystalline domain thickness.

4. Conclusions

Changes in phase composition, (namely the amounts of rigid fraction/crystallinity, semirigid, and soft fractions), molecular mobility and domain thickness of both annealed and nonannealed iPP samples were investigated by ^{1}H NMR, SAXS, and DSC at different temperatures and different annealing times. The amounts of the rigid fraction as determined by NMR, crystallinity from DSC and SAXS exceeds by 5−10%. This difference can be quantitatively explained by the effect of the interface, which is not taken into account in the analysis of the DSC and SAXS data.

According to TEM, the morphology of nonannealed iPP is mainly lamellar. For iPP samples that are annealed at different temperatures and different times, the cross-hatching morphology can be observed. However, the predominant morphology remains lamellar. This is confirmed by the comparison of the phase composition with the domain thickness ratio that is determined by simulations of the results of the spin-diffusion data using 1D, 2D, and 3D solutions of the spin-diffusion equations. In approximation of two-phase model, the long period obtained by NMR and SAXS is in good agreement with each other.

An important feature of the spin-diffusion experiments reported in this investigation is the temperature dependence of the proton spin diffusivities, which decrease with increasing the temperature. The temperature dependence of the spin diffusivity of the amorphous phase was derived from the spectral line width. In the approximation of a single correlation time described by the Williams−Landel−Ferry (WLF) equation, the temperature dependence of the spin diffusivities was established, and the obtained WLF coefficients are in the range that is typical for the amorphous phase in semicrystalline polymers and amorphous polymers.

The thicknesses of the rigid domains for iPP that is annealed at different temperatures and different times is discussed as a function of the logarithm of the annealing time. A linear relationship holds for all cases in good agreement between theory predictions and the experimental results for other polymers.[68,71]

The existence of the phenomenological correlation between microscopic and mesoscopic properties of iPP is reported. Microscopic properties are described by ^{1}H transverse relaxation rates or second van Vleck moment characterizing mainly the proton dipolar network. The morphology and domain thickness characterize the polymer on the mesoscopic scale. The correlation is complex and explained by the improvement of the crystalline order during the crystal thickening.

Acknowledgment. This study was sponsored by SABIC Europe BV. C.H. gratefully acknowledges SABIC Europe BV for a Ph.D. grant. The authors are grateful to Rudy Deblieck for helpful discussions.

References and Notes

(1) Popli, R.; Mandelkern, L. *J. Polym. Sci., Polym. Phys.* **1987**, *25*, 441−449.
(2) Halpin, J. C.; Kardos, J. L. *J. Appl. Phys.* **1972**, *43*, 2235.
(3) Boyd, R. H. *Polym. Eng. Sci.* **1979**, *19*, 1010.
(4) Boyd, R. H. *J. Polym. Sci., Polym. Phys.* **1983**, *21*, 493.
(5) Strobl, G.; Schneider, M. *J. Polym. Sci., Polym. Phys.* **1980**, *18*, 1343.
(6) Mandelkern, L. *Crystallization of polymers*; McGraw-Hill: New York, 1964.

(7) Mandelkern, L. *Polym. J* **1985**, *17*, 337.
(8) Negahban, M.; Wineman, A. S. *Int. J. Eng. Sci.* **1992**, *30*, 819.
(9) Wortmann, F. J.; Schulz, K. V. *Polymer* **1996**, *37*, 819.
(10) Boyd, R. H. *Polymer* **1985**, *26*, 323.
(11) Boyd, R. H. *Macromolecules* **1984**, *17*, 903.
(12) Bellare, A.; Cohen, R. E.; Argon, A. S. *Polymer* **1993**, *34*, 1393.
(13) Goschel, U.; Deutscher, K.; Abetz, V. *Polymer* **1996**, *37*, 1.
(14) Hikosaka, M.; Amano, K.; Rastogi, S.; Keller, A. *Macromolecules* **1997**, *30*, 2067.
(15) Alamo, R. G.; Brown, G. M.; Mandelkern, L.; Lehtinen, A.; Paukkerri, R. *Polymer* **1999**, *40*, 3933.
(16) Akizadeh, A.; Richardson, L.; Xu, J.; McCartney, S.; Marand, H.; Cheung, Y. W.; Chum, S. *Macromolecules* **1999**, *32*, 6221.
(17) Marand, H.; Alizadeh, A.; Farmer, R.; Desai, R.; Velikov, V. *Macromolecules* **2000**, *33*, 3392.
(18) Iijima, M.; Strobl, G. *Macromolecules* **2000**, *33*, 5204.
(19) Maiti, P.; Hikosaka, M.; Yamada, K.; Toda, A.; Gu, F. *Macromolecules* **2000**, *33*, 9069.
(20) Weglarz, W. P.; Peemoeller, H.; Rudin, A. *J. Polym. Sci., B: Polym Phys* **2000**, *38*, 2487.
(21) Alizahedh, A.; Sohn, S.; Quinn, J.; Marand, H.; Shank, L. C.; Iler, H. D. *Macromolecules* **2001**, *34*, 4066.
(22) Labour, T.; Gauthier, C.; Seguela, R.; Vigier, G.; Bomal, Y.; Orange, G. *Polymer* **2001**, *42*, 7127.
(23) Mandelkern, L.; Allou, A. L.; Gopalan, M. *J. Phys. Chem.* **1968**, *72*, 309.
(24) Mathot, V. B. F. *Calorimetry and Thermal Analysis of Polymers*; Munich, Germany, Vienna and New York, 1944.
(25) Chiang, R.; Flory, P. J. *J. Am. Chem. Soc.* **1961**, *83*, 2857.
(26) Ruland, W. *Acta Crystallogr.* **1961**, *14*, 1180.
(27) Ruland, W. *Polymer* **1964**, *5*, 89.
(28) Vonk, C. G. *J. Appl. Crystallogr.* **1973**, *6*, 81.
(29) Kavesh, S.; Schultz, J. M. *J. Polym. Sci., Part A-2* **1971**, *9*, 85.
(30) Wunderlich, B. *Thermal analysis of polymeric materials*; Springer, Berlin, 2005.
(31) Bergmann, K.; Nawotki, K. *Z.-Z. Polym* **1967**, *219*, 132.
(32) Kitamaru, R.; Horii, F.; Hyon, F. *J. Polym. Sci., Polym Phys* **1977**, *15*, 821.
(33) Kitamaru, R.; Horii, F. *Adv. Polym. Sci.* **1978**, *26*, 139.
(34) Earl, W.; VanderHart, D. L. *Macromolecules* **1979**, *12*, 762.
(35) Tanaka, H.; Kohrogi, F.; Suzuki, K. *Eur. Polym. J.* **1989**, *25*, 449.
(36) Dadayli, D.; Harris, R. K.; Kenwright, A. M.; Say, B. J.; Sunnetcioglu, M. M. *IRC Polym. Technol.* **1994**, *35*, 4083.
(37) Schreurs, S.; Francois, J. P.; Adriaenens, P.; Gelan, J. *J. Phys. Chem. B* **1999**, *103*, 1393.
(38) Tanaka, H.; Inoue, Y. *Polym. Int.* **1993**, *31*, 9.
(39) Isasi, J. R. L.; Mandelkern, M. J.; Alamo, R. G. *J. Polym. Sci., Polym. Phys.* **1999**, *37*, 323.
(40) McBrierty, J. V.; Paker, K. J. *Nuclear Magnetic Resonance in Solid Polymers*; Cambridge Univ. Press: Cambridge, U.K., 1993.
(41) Packer, K. J.; Pope, J. M.; Yeung, R. R. *J. Polym. Sci., Polym. Phys.* **1984**, *22*, 589.
(42) Hu, W. G.; Schmidt-Rohr, K. *Polymer* **2000**, *41*, 2979.
(43) Buda, A.; Demco, D. E.; Bertmer, M.; Blümich, B.; Litvinov, V. M.; Penning, J. P. *J. Phys. Chem. B* **2003**, *107*, 5357.
(44) Buda, A.; Demco, D. E.; Blümich, B.; Litvinov, V. M.; Penning, J. P. *ChemPhysChem* **2004**, *5*, 876.
(45) VanderHart, D. L.; McFadden, G. B. *Solid State Nucl. Magn. Reson.* **1996**, *7*, 45.
(46) Eckman, R. R.; Henrichs, P. M.; Peacock, A. J. *Macromolecules* **1997**, *30*, 2474.
(47) Buda, A.; Demco, D. E.; Bertmer, M.; Blümich, B.; Reining, B.; Keul, H.; Höcker, H. *Solid State Nucl. Magn. Reson.* **2003**, *24*, 39.
(48) Ba, Y.; Ripmesster, J. A. *J. Chem. Phys.* **1998**, *108*, 8589.
(49) Cherry, B. R.; Fujimito, C. H.; Cornelius, C. J.; Alam, T. M. *Macromolecules* **2005**, *38*, 1201.
(50) Goldman, M.; Shen, L. *Phys. Rev.* **1961**, *144*, 321.
(51) Demco, D. E.; Johansson, A.; Tegenfeldt, J. *Solid State Nucl. Magn. Reson.* **1996**, *7*, 17.
(52) Hedesiu, C.; Demco, D. E.; Kleppinger, R.; Buda, A. A.; Blumich, B.; Remerie, K.; Litvinov, V. M. *Polymer* **2007**, *48*, 763.
(53) Litvinov, V. M.; Penning, J. P. *Molecular Chem. Phys.* **2004**, *205*, 1721.
(54) Schneider, M.; Gaspar, L.; Demco, D. E.; Blumich, B. *J. Chem. Phys.* **1999**, *111*, 402.
(55) Litvinov, V. M.; Soliman, M. *Polymer* **2005**, *46*, 3077.
(56) Pyda, M., Ed. ATHAS Data Bank. http://web.utk.edu/∼athas/databank/, 1994.
(57) Schmidt-Rohr, K.; Spiess, H. W. *Multidimensional Solid-State NMR and Polymers*; Academic Press: London, 1994.
(58) Ito, J.; Mitani, K.; Mizutani, Y. *J. Appl. Polym. Sci.* **1992**, *46*, 1221.
(59) Abragam, A. *The Principles of Nuclear Magnetism*; Oxford University Press: Oxford, U.K., 1961.
(60) Strobel, G. *The Physics of Polymers*; Berlin, New York, Barcelona, Spain, and Tokyo 1997.
(61) Voda, A. M.; Demco, D. E.; Voda, A.; Schauber, T.; Adler, M.; Dabisch, T.; Adams, A.; Baias, M.; Blümich, B. *Macromolecules* **2006**, *39*, 4802.
(62) Wang, J. *J. Chem. Phys.* **1996**, *104*, 48.
(63) Brandrup, J.; Immergut, E. H.; Grulke, E. A. *Polymer Handbook*; 1999.
(64) Poussin, L.; Bertin, Y. A.; Parisot, J.; Brassy, C. *Polymer* **1998**, *39*, 4261.
(65) Schmidt-Rohr, K.; Spiess, H. W. *Macromolecules* **1991**, *24*, 5288.
(66) Martorana, A.; Piccarolo, S.; Sapoundjieva, D. *Macromol. Chem. Phys.* **1998**, *3*, 531.
(67) Ferrero, A.; Ferracini, E.; Hosemann, R. *Polymer* **1984**, *25*, 1747.
(68) Sanchez, I. C.; Colson, J. P.; Egy, R. K. *J. Appl. Phys.* **1973**, *44*, 4332.
(69) Statton, W. C. *J. Appl. Phys.* **1961**, *32*, 2332.
(70) Fischer, E. W.; Schmidt, G. F. Z. *Angew. Chem.***1962**, *1*, 488.
(71) Sanchez, I. C.; Peterlin, A.; Egy, R. K.; McCrackin, F. L. *J. Appl. Phys.* **1974**, *45*, 4216.
(72) Peterlin, A. *J. Polym. Sci., Part B: 1* **1963**, *B1*, 279.
(73) Peterlin, A. *Polymer* **1967**, *6*, 25.
(74) Yamada, K.; Hikosaka, M.; Toda, A.; Yamazaki, S.; Tagashira, K. *Macromolecules* **2003**, *36*, 4790.

MA070014Q